Identification of exciton-exciton annihilation in hematite thin films

Alexander T. Paradzah, Kelebogile Maabong, Huzifa M. A. M. Elnour, Asmita Singh,

Mmantsae Diale, and Tjaart P. J. Krüger*

Department of Physics, University of Pretoria, Private Bag X20, Hatfield 0028, South Africa.

Corresponding Authors

Tjaart P. J. Krüger, Email:tjaart.kruger@gmail.com

ABSTRACT

Hematite, a common type of iron oxide, is a promising material for solar technologies, due to its small bandgap that allows for solar radiation absorption in the visible region, low toxicity in aqueous solutions, easy synthesis and natural abundance. However, fast electron–hole recombination has been hampering full applicability of hematite in solar technologies. In this study, we used visible femtosecond transient absorption spectroscopy to investigate the excited-state decay and electron–hole recombination dynamics of nanostructured hematite thin films. By varying the pump excitation fluence and performing global and target data analysis, we identified the presence of nonlinear decay processes during the initial picosecond after photoexcitation, which have a non-negligible contribution at pump fluences of $>\sim 1$ mJ/(pulse·cm^2). Calculations show exciton-exciton annihilation to be the dominant nonlinear process, with an average rate constant of 7.09×10^{-9} cm^3 s^{-1}. Annihilation calculations also allowed us to estimate the annihilation radius to be 2.3 nm, thus explaining the rapid exciton-exciton annihilation in the immediate aftermath of photoexcitation. Probe

wavelength-dependent decay dynamics points to excitation energy redistribution and involvement of traps in the recombination dynamics. We finally present a kinetic model, verified by performing target data analysis, showing the rates and channels of the dominant processes involved with electron–hole recombination upon relatively high excitation rates. The extremely fast electron–hole recombination process in hematite is one of the main reasons hindering the full applicability of the material in solar water splitting. Measures to limit these ultrafast recombination processes should, therefore, be incorporated into device fabrication and preparation to further improve the material.

1 Introduction

The drive towards cleaner renewable energy has become inevitable due to fast depletion of fossil fuels and the associated carbon footprint. This has led to extensive research on different renewable energy technologies, particularly solar energy, which is the cheapest and most abundant alternative. Although several materials are already in use for solar energy harnessing, the commonly used materials such as silicon have low energy conversion efficiencies. Due to the seasonal nature of sunlight, it has become imperative to utilize other ways of harnessing and storing solar energy. Water splitting, also known as artificial photosynthesis, has emerged as an enticing concept of converting solar energy into storable fuels. It makes use of semiconductor photoanodes that create electron-hole (e^--h^+) pairs upon photo-illumination. The e^--h^+ pairs are then utilized in reduction and oxidation reactions that lead to the splitting of water into its constituent elements, oxygen, and hydrogen. This way of hydrogen production is particularly attractive as it is environmentally friendly and hydrogen is a storable fuel. The process of water splitting was first demonstrated by Honda and Fujishima in the early 1970s[1] using a titania (TiO_2) photoanode. A significant amount of research has since been performed to making the process more efficient. Currently, more emphasis is laid on the use of metal oxide semiconductors for photoanodes[2-3].

Several metal oxides such as TiO_2, tungsten trioxide (WO_3), bismuth vanadate ($BiVO_4$) and zinc oxide (ZnO) have been studied extensively for potential use in solar-cell and water-splitting technologies[4-8]. TiO_2 first appeared as an ideal metal oxide for water splitting mainly due to excellent stability in aqueous solutions. Additionally, TiO_2 conduction and valence bands straddle the water redox potentials – a crucial requirement for oxygen and hydrogen production through water splitting[9]. However, the efficiency of TiO_2-based photoanodes is very low due to its large bandgap, which highly limits visible solar absorption. The same

problem of limited visible light absorption also hampers the efficiency of other large bandgap metal oxide semiconductors such as WO_3[10] and ZnO[7]. Hematite, best known as α-Fe_2O_3 (Fe_2O_3 hereafter), is a metal oxide semiconductor with a relatively narrow bandgap of ~2.1 eV and can thus absorb substantially in the visible region of the solar spectrum reaching the earth's surface[11-13]. Despite the excellent properties, the full applicability of Fe_2O_3 in water splitting is greatly limited by ultrafast e^--h^+ recombination, short hole diffusion lengths of 2 to ~20 nm[14-15], and low conductivity[16]. These shortfalls consequentially lead to low solar to photocurrent conversion efficiency [17]. Several methods such as elemental doping[18], bandgap engineering[19] and use of heterojunctions or interfacial layers[10, 20] can be used to counter these shortfalls.

It is without doubt that the rate of e^--h^+ recombination following photoillumination of a semiconducting material is an important indicator of whether a material can be sustainably used in solar technology, particularly in solar water oxidation. Several studies have been carried out before to determine the e^--h^+ recombination rates on hematite under water splitting conditions, under applied external voltage bias or in air[21-23]. The results revealed that Fe_2O_3 undergo rapid e^--h^+ recombination on timescales of a few hundred femtoseconds[24-26] to a few microseconds when an external voltage is applied[27]. These measurements were performed on nanostructures of different geometries, such as nanowires, nanorice, spheroidal nanoparticles, and also with different dopants to prolong the carrier lifetimes. Electron-hole recombination in most semiconductor materials, especially those with reduced dimensionality, can be accelerated by nonlinear processes such as three-particle Auger recombination, bimolecular (exciton-exciton) Auger recombination (also known as exciton–exciton annihilation, EEA) and biexciton formation. These nonlinear processes may occur concurrently or separately, and can be caused in ultrafast studies by high pump fluences that lead to multiple exciton formation.

In semiconductors that have a large density of trap states, the probability for nonlinear processes increases dramatically after the trap states are filled. To the best of our knowledge, not much work has as yet been done to determine the effect of excitation fluence variations on the excited-state decay and recombination lifetimes in hematite nanostructures. Cherepy *et al.*[17] carried out fluence-varying measurements on Fe_2O_3 nanostructures up to a total fluence of 1.2 mJ/(pulse·cm^2) and did not observe any fluence-dependent decay dynamics. Similarly, no fluence-dependent dynamics were observed by Sorenson *et al.*[24] after varying the pump fluence from 0.15 to 1.8 mJ/(pulse·cm^2). However, Pendlebury *et al.*[27] observed a retardation of the decay kinetics of hematite nanoparticles by decreasing the excitation densities from 360 down to 15 μJ(pulse·cm^2), attributing the effect to nongeminate bimolecular recombination. These studies create a discrepancy where low excitation densities produced fluence-dependent decay dynamics and higher fluences did not. In this study, we investigated this inconsistency by carrying out femtosecond pump-probe spectroscopy measurements on nanostructured Fe_2O_3 thin films using high pump fluences. We performed global analysis on the transient data to investigate the effect of excitation pump fluence values from 1.40 to 4.19 mJ/(pulse·cm^2) on the spectral kinetic rates and used annihilation calculations to show that the rate changes are correlated with EEA.

2   Materials and Methods

2.1   Hematite synthesis

Hematite thin films were deposited by spin coating onto conductive fluorine-doped tin oxide (FTO, TEC 8, Pilkilton) glass substrates. FTO substrates were pre-cleaned ultrasonically in acetone, ethanol and deionized water for 5 min, followed by rinsing with ethanol and dried

with nitrogen gas. The precursor solution of iron-oleate was prepared from a mixture of iron (III) nitrate (Fe(NO$_3$)$_3$·9H$_2$O, ≥98%, Sigma Aldrich) and oleic acid (C$_{18}$H$_{34}$O$_2$, ≥99% GC, Sigma Aldrich). Three drops of the solution were placed on the cleaned substrate and spun off at a high speed of 3000 rpm for 30 s, then dried at 90°C on a hot plate before being annealed in a furnace at 500°C for 30 min. Three thin film layers of hematite were obtained by repeated deposition, drying and heat treatment steps for each layer at a time.

2.2   Measurements

The thin films had a total average thickness of ~450 nm, as measured using a P-15KLA Tencor stylus surface profiler. Powder X-ray diffraction (XRD) (PAN analytical X'Pert PRO) was performed in order to confirm the structure, phase and crystallinity of hematite thin films. Surface morphology of the nanostructures was investigated using field emission scanning electron microscopy (FE-SEM, ZEISS SEM-Microscopy). The absorbance of hematite thin films was measured using an Ocean Optics spectrometer (USB4000 series).

Transient absorption spectroscopy measurements were performed using the setup previously described[20]. Briefly, we used a Ti: Sapphire amplified laser system (150 fs pulse duration; 775 nm peak wavelength; 1 kHz repetition rate). An output averaging 850 mW was split into two beams, 30% pump and 70% probe. The pump beam was directed into a β-barium borate (BBO) crystal for frequency doubling to produce a 387.5 nm (3.2 eV) centred beam with a FWHM bandwidth of ∼4 nm. The 387.5 nm pump beam was then focussed into a sample using a telescope, and neutral density filters were used to attenuate the pump power where different pump fluences were required. A chopper was inserted in the pump beam path to enable "pumped" and "unpumped" measurements. The pump beam was estimated to have a pulse duration of ~180 fs just before the sample. Different pump-probe delay times were obtained by passing the probe beam through a motorized translation stage. A maximum of 2

ns probe delay can be achieved on our setup, although in this study we limited the delay to 50 ps since we were interested in the earliest electron-hole dynamics post excitation. After the delay line, the probe beam was attenuated and focussed into a sapphire crystal to produce a white light continuum, which was split using a 50/50 beam splitter. One part of the supercontinuum was used as the probe and focussed into the sample, overlapping temporally and spatially with the pump beam, while the other part, the reference beam, was directed also through the sample but without overlapping with the pump. The reference was used to account for fluctuations occurring in the probe, which may otherwise be mistaken for pump-induced dynamics. The pump and probe beam diameters were ~500 μm and ~300 μm, respectively, as measured using a ThorLabs DCC1545 CMOS camera. Using a probe beam that is smaller in size than the pump beam ensured that all probed sections of the samples had been pumped. Upon interaction of the sample with the probe beam, processes such as ground state bleaching (GSB), excited state absorption (ESA) of electrons and holes, and stimulated emission (SE) can be observed. Beyond the sample, both the probe and the reference beams were focussed into optical fibres and directed to a diffraction grating, which dispersed the beams onto a photodiode array to measure spectra, using ExciPro software.

2.3   Data analysis

Global analysis of the data was performed using Glotaran, a global and target data analysis program[28]. In Glotaran, all wavelengths are analyzed simultaneously using a common set of kinetic parameters as opposed to wavelength- or time-specific data fitting. A sequential model was used for the analysis. A sequential model provides a more appropriate description of the recombination dynamics in semiconductors than a parallel decay model because electrons first relax to the conduction band edge from higher excited states initially populated by the pump pulse, followed by either direct or trap-mediated recombination with the valence

holes in a sequential fashion. Although other processes such as trapping and recombination from the conduction band edge might appear to favour a parallel model, sequential dynamics are more dominant. It is important to note, however, that both the sequential and parallel decay models yield similar decay/recombination lifetimes (i.e., the two models are mathematically equivalent). In a sequential model (1 → 2 → 3 → ….), each number represents an evolution-associated difference spectrum (EADS), which interconvert, as indicated by the arrows, with successive monoexponential decay times (τ_1, τ_2, τ_3,...). EADS 1 is considered to decay into EADS 2 with decay time τ_1, while EADS 2 has lifetime τ_2 and decays into EADS 3, etc. The first EADS represents the zero-time spectra, i.e., it shows the populations of the excitation energy prior to any relaxation, energy transfer or recombination processes. From target analysis, one obtains species associated difference spectra (SADS). The SADS represents pure states as opposed to EADS which define the spectral evolution of the entire system. Inverses of rate constants used in target analysis give the characteristic time of transitions between particular compartments (species).
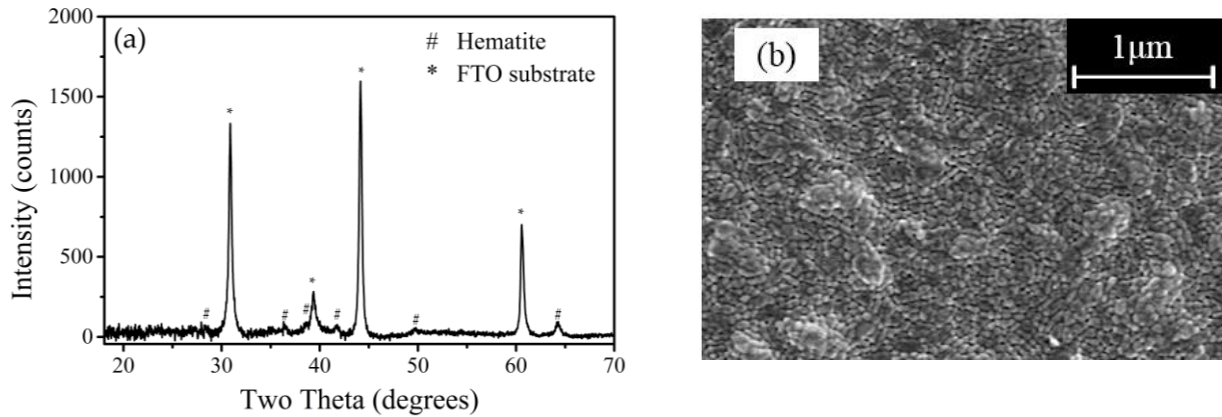
3   Results

3.1   Structural characterization

The XRD pattern for the hematite thin films (Figure 1a) confirms that the α-phase of hematite was produced with high purity (JCPDS 33-0664). The α-Fe_2O_3 peaks are not very prominent because the nanostructure films were considerably thin. The less prominent peaks may also be due to the small-sized nature of the nanostructures, which is clearly supported by SEM in Figure 1b. All other peaks originate from the FTO substrate. FE-SEM micrographs (Figure 1b) show a uniform covering of the FTO substrate by the hematite nanostructures. It can be observed from the micrographs that the nanoparticle size is uniform and ~60 nm, on average.

The sizes were confirmed using the Scherrer formula of the peak width analysis on the XRD results. We considered the thin film uniformity and purity to be ideal for ultrafast pump-probe spectroscopic measurements.


Figure 1. (a) XRD spectrum confirming the presence of hematite in the thin films. α-Fe_2O_3 peaks are marked with a "#" while the peaks marked with a "*" belong to the FTO substrate. (b) FE-SEM micrographs for hematite thin film.

3.2 Steady-state absorption results

The top of the Fe_2O_3 valence band is composed of mixed Fe 3d and O 2p states with predominantly O 2p character[29]. The absorption spectrum of hematite is thus composed of optical transitions from these two states to the conduction band, which is predominantly composed of Fe 3d-like states[29]. The absorption spectrum of the hematite thin film on an FTO substrate (Figure 2) shows an absorption maximum at ~390 nm (~3.18 eV), which is attributed to ligand-to-metal charge transfer (LMCT) from O 2p orbitals to Fe^{3+} $2t_{2g}$ and $3e_g$ orbitals[12, 30]. It is important to note, however, that other absorption maxima exist at wavelengths below 390 nm (not shown). In particular, a maximum has been observed at ~230 nm and attributed largely to LMCT[12, 31], and to a lesser extent to Fe^{3+} ligand field transitions[32]. The absorption features at wavelengths between ~387.5 nm and ~590 nm result

from weak Fe d-d ligand field transitions[31]. Even though d-d transitions are both spin and Laporte forbidden[12], they still weakly contribute to absorption due to magnetic coupling of electronic spins of nearest-neighbour Fe^{3+} cations[33]. At wavelengths above ~590 nm, the observed absorption tail is a result of sub-bandgap states since band-to-band transitions are not possible at energies below ~2.1 eV (~590 nm).
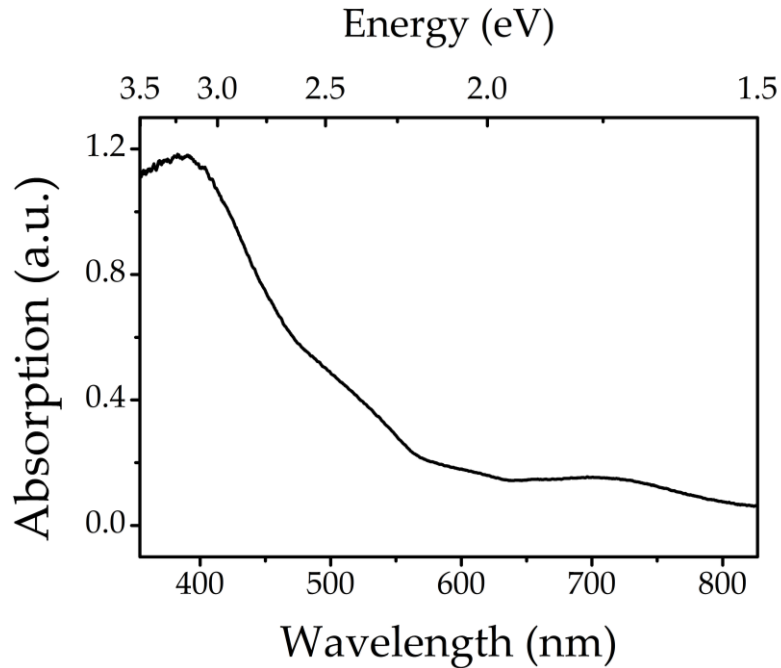

Figure 2. The absorption spectrum of α-Fe_2O_3 thin film showing a maximum absorption at ~390 nm.

3.3   Transient absorption results

The time-dependent behaviour of the transient absorption spectra following an excitation pump fluence of 1.40 mJ/(pulse·cm^2) is shown in Figure 3a. Spectra corresponding to higher pump fluences are displayed in Figure S1. The negative amplitude of the spectra at wavelengths below ~470 – 490 nm (above ~3.05 – 2.53 eV) is the result of GSB and SE. The excessive width of the GSB/SE signal is directly related to the broad absorbance band (Figure 2). Put differently, excitation by the pump pulse results in a broad energy distribution of electrons and holes in the conduction and valence bands, respectively, which reduces

absorption of the probe pulse over a broad range of energies, giving rise to a broad, negative bleach signal. Above ~470 – 490 and ~505 nm (below ~2.53 – 3.05 and ~2.46 eV), the spectra are positive. The amplitude increases first gradually, then steeply beyond ~525 nm (below ~2.36 eV), forming a broad, positive band with a maximum at ~570 nm (~2.18 eV) and a broad tail extending beyond 650 nm (below 1.91 eV).

This dominant, broad, positive band originates from ESA, specifically absorption of the probe light by photoexcited holes in the valence band and photoexcited electrons in the conduction band. Excited hole absorption was proposed to be the main cause, based on measurements of hematite thin films subjected to an anodic bias, thus controlling the accumulation of holes in the valence band and monitoring the growth or decay of the ~570 nm peak as the bias was varied[23, 36]. However, in another study where the transient absorption signals were compared with the calculated electronic band structure of hematite, the whole positive band was attributed to mainly excited electron absorption[24]. The latter assignment was based on a comparison of the transient absorption spectral properties with the valence and conduction band sizes and energy gaps, as well as an estimation of the density of states of the bands and the dipole strength of intra-band transitions, arguing that the latter two properties are greater for electron transitions in the conduction band. Although these results indicate the meaningful contribution of electron absorption towards the ESA signal, two other important considerations not adequately accounted for in the interpretation are the gap between the two lowest conduction bands that are populated by electrons and the valence band being broader than the combined conduction bands. Both considerations relate to increased hole absorption as opposed to electron absorption, in particular at higher energies (shorter wavelengths). In another study, the ESA feature was attributed to the presence of localized intra-bandgap states[34].
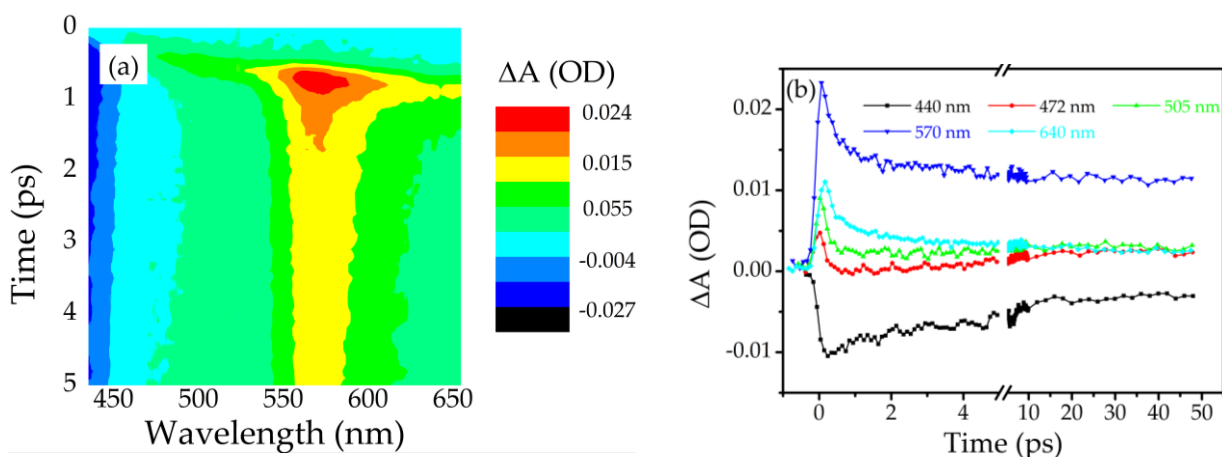
Figure 3. (a) Transient absorption difference spectra obtained at a pump fluence of 1.40 mJ/(pulse·cm^2) centred at 387.5 nm, shown until a delay time of 5 ps. (b) Kinetic traces at specified wavelengths, shown until a delay time of 20 ps.

Transient kinetics at selected wavelengths are shown in Figure 3b, illustrating the dynamics of the main difference absorption features. All features grew rapidly, reaching a maximum in <100 fs, although the 440-nm and 640-nm kinetics are comparatively slower. The kinetics also helps in visualizing the decay rates of selected spectral features. The decay of the positive band peaking at ~570 nm is fast initially and slows down after ~1 ps. Similar spectral decay dynamics are observed at the other presented wavelengths. Around 472 nm, the spectrum becomes bipolar, i.e., it contains negative and positive features, pointing to a wavelength-dependent interplay between the GSB and ESA decay kinetics, as explained below.

Singular value decomposition of the data indicated that at least three different lifetimes were required to adequately describe the spectral decays. We thus performed global data analysis using a three-component sequential model. The obtained EADS represent the spectral evolution of the whole system and not that of pure spectral states. The EADS corresponding with each of the utilized fluences are shown in Figure S2. Although the spectral features are

12

largely similar, the associated decay lifetimes displayed a clear fluence-dependent decrease (Table 1). We will consider the fluence dependence of each lifetime in more detail.

With pump pulses of 3.2 eV, electrons can be excited from the top of the valence band to the bottom of the second conduction band[24] as well as from a broad range of energies below the valence band maximum to the first conduction band. In fact, any transition separating photogenerated e^--h^+ pairs by 3.2 eV is permissible. These hot electrons and holes relax to the band edges on an ultrafast timescale. The initial decay lifetime is therefore attributed to hot carrier cooling, i.e., both hot electron relaxation to the conduction band edge and hole diffusion to the top of the valence band. Previous studies[17, 35] have claimed that these initial, sub-ps processes are independent of the pump fluence. However, in the present study, using somewhat higher fluences, a marked fluence dependence can be observed (Table 1). Specifically, a factor of 3 increase in pump fluence resulted in a 2.3 times shortening of the initial decay lifetime, τ_1. This indicates that electron and hole relaxation to the respective band edges are not the only processes featuring on sub-ps timescales. Since the timescales for band-to-band e^--h^+ recombination or defect-assisted recombination in hematite, in the absence of nonlinear processes like three-particle Auger recombination and EEA, were shown to be in the order of several ps to ns[24, 36-37], recombination occurring on a sub-ps timescale (i.e., corresponding mainly with τ_1) suggests the presence of nonlinear processes.

The fluence dependency was even more noticeable in the second lifetimes, τ_2 (Table 1), showing a 3.2 times shortening of the lifetime with a 3 times increase in fluence. Since the decay is in the ps range, we attribute this lifetime to both e^--h^+ recombination and electron trapping by midgap (MG) states. The fluence dependency observed for the second lifetime also suggests the presence of nonlinear processes operating on a sub-ps to few-ps timescale. The fluence-dependent decay can be visualized more clearly with kinetic traces. Figure 4 shows the traces at 570-nm and 440-nm. Since the transient signal at 570 nm is largely believed to

emanate from excited hole absorption[22, 38-39] and likely also excited electron absorption[24], its decay should be an acceptable representation of the overall recombination dynamics. The accelerated decay of the 570-nm trace at higher fluences (Figure 4a) indicates that the fast recombination of e^--h^+ pairs could be facilitated by nonlinear processes. This will concomitantly lead to enhanced decay in the bleach signal, thus explaining the accelerated decay of the 440-nm signal at higher fluences (Figure 4b).

Table 1. Decay lifetimes obtained for the respective pump fluences obtained from global analysis. An instrument response function of 180 fs was incorporated in the data analysis to calculate the sub-ps lifetimes more accurately.

	1.40 mJ/(pulse·cm^2)	1.96 mJ/(pulse·cm^2)	2.51 mJ/(pulse·cm^2)	4.19 mJ/(pulse·cm^2)
τ_1	425 fs	380 fs	250 fs	185 fs
τ_2	5.36 ps	4.52 ps	2.72 ps	1.65 ps
τ_3	5.5 ns	4.7 ns	3.8 ns	3.2 ns

The third lifetime (τ_3) was observed to decrease more slowly with increasing pump fluence than the other two lifetimes. It is unlikely that nonlinear processes play a role at such long lifetimes since traps drastically reduce the exciton concentration on a timescale of a few ps. This lifetime should correspond to direct recombination, involving, in particular, those electrons that undergo back-flow from the FTO.
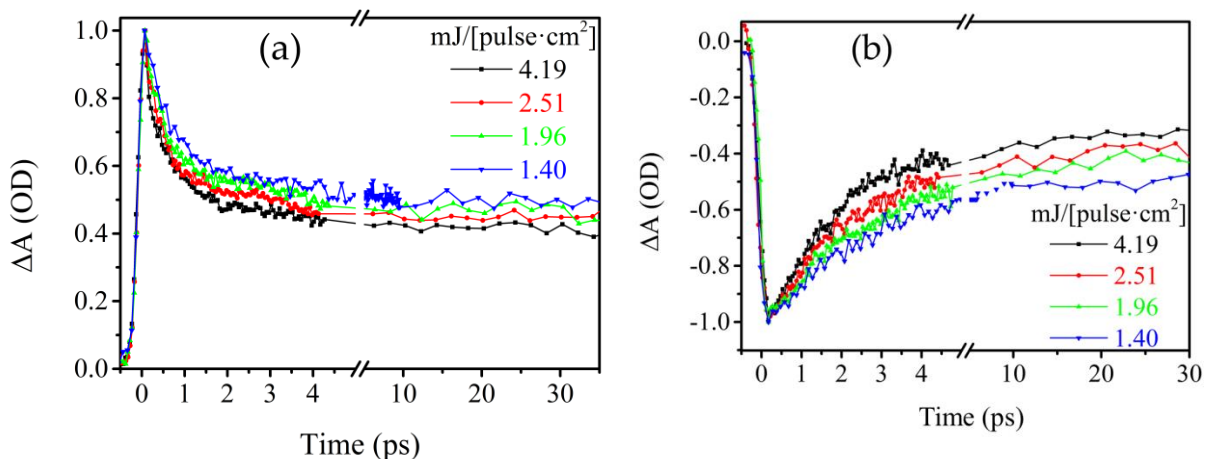
Figure 4. Normalized traces at 570 nm (a) and 440 nm (b) at different excitation fluences. Faster decay observed following higher pump fluences indicates the presence of nonlinear processes.

The presence of nonlinear processes is also reflected in Figure 5, showing the fluence dependence of the maximum amplitude of the ESA signal at different probe delays. Although the data follow a linear trend, the fits pass above the origin, suggesting rather a quadratic dependence of the amplitude on the pump fluence. The data corresponding with the longest delay shows the flattest slope and can be explained by the accumulative effect of non-linear processes during the first few ps. It is noteworthy that in a similar study using lower pump fluences, most of the linear fits also intercepted the y-axis above the origin[24].
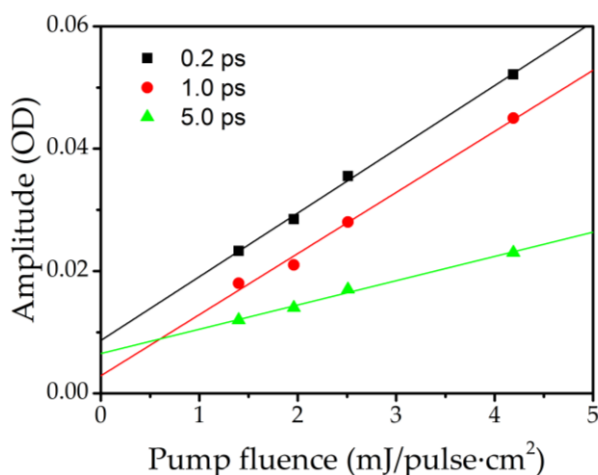
Figure 5 Dependence of the maximum amplitude (near 570 nm) of the difference absorption spectra on the pump fluence for different probe delays.

15

3.4 Probe wavelength dependent decay

The decay lifetimes were also found to vary with the probe wavelengths, specifically for the red wing of the broad, positive 570 nm band. For each of the four pump fluences, we fitted the 570-nm and 640-nm kinetic traces separately, using a biexponential decay function. All decay rates were slower at the shorter wavelength (Figure S3 and Table 2). This can be explained by the high density of Fe^{3+} trap states in hematite[17, 40] favouring trapping of electrons from the conduction band to low-energy states, causing a spectral blue shift and thus wavelength-dependent decay rates[17]. It can also be deduced from this observation that trap-assisted recombination occurs faster than band-to-band recombination. Recombination occurring at wavelengths longer than 600 nm has to be trap-assisted; otherwise, the energy is too low for direct recombination.

Table 2. Decay lifetimes of transients at 570-nm and 640-nm obtained from biexponential fits.

	1.40 mJ/(pulse·cm^2)	1.96 mJ/(pulse·cm^2)	2.51 mJ/(pulse·cm^2)	4.19 mJ/(pulse·cm^2)
$\tau_{1, 570\ nm}$	496 fs	417 fs	305 fs	226 fs
$\tau_{2, 570\ nm}$	6.12 ps	5.62 ps	2.72 ps	2.01 ps
$\tau_{1, 640\ nm}$	422 fs	394 fs	283 fs	202 fs
$\tau_{2, 640\ nm}$	5.87 ps	4.52 ps	2.51 ps	1.74 ps

4 Discussion

4.1 Annihilation calculations

Following the observed pump fluence-dependent dynamics and presence of e^--h^+ recombination at sub-ps timescales, there is sufficient reason to expect the presence of nonlinear processes at these timescales. Possible nonlinear processes following high pump fluences include EEA, three-particle Auger recombination and biexciton formation. Formation of biexcitons can be ruled out in the present study due to the lack of a characteristic signal that can be attributed to biexciton formation. The presence of biexciton formation can be observed by the appearance of a low-energy emission signal, which generally occurs at very high pump fluences[41-42]. For systems where the three-particle Auger recombination process is dominant, graphs of $(\Delta A_0 / A_t)^2 - 1$ vs. delay time should yield straight lines with decreasing slope as the fluence is increased[43]. Here, ΔA_0 is the maximum amplitude of the difference absorption spectra, while ΔA_t is the corresponding amplitude at delay time t. Although we observed a linear dependency with a different slope before and after 1 ps (Figure S4), the slopes do not show any dependence on the fluence, except for the slight increase in the slope for the highest fluence after 1 ps, which is opposite to the expected behaviour for three-particle Auger recombination. The presence of three-particle Auger recombination can therefore be ruled out.

Next, we investigate the influence of EEA. The rate equation for exciton density, when dominated by EEA in solids, can be described by[44]

$$\frac{dN}{dt} = -\frac{N}{\tau} - \gamma_{eea}N^2,$$
(1)

where N is the exciton population at a time t after excitation, τ is the exciton decay lifetime in the absence of EEA and γ_{eea} is the annihilation rate constant. The analytical solution to the equation is obtained as

$$N(t) = \frac{N_0\exp(-t/\tau)}{1+\gamma_{eea}\tau N_0[1-\exp(-t/\tau)]} \, , \qquad (2)$$

where N_0 is the initial exciton population. A linear relation exists between the transient absorption amplitude and the density of generated excitons such that[45] $\Delta A_0/\Delta A_t = N_0/N(t)$. N_0 is obtained using the relation

$$N_0 = \frac{E\lambda}{Vhc}(1-10^{-A}), \qquad (3)$$

where E is the pulse energy, V is the volume of the photo-excited thin film, λ is the excitation wavelength, A is the absorbance of the thin film, h is Planck's constant, and c is the speed of light in vacuum.

A linear relationship between $1/N(t)$ and $\exp(t/\tau)$ is observed within the first 1.2 ps (Figure 4a), with a decreasing slope as the pump fluence increases. This trend is a clear indication that EEA plays an important role during the initial ps following photoillumination at all the investigated fluences. At ~1.2 ps, the slope flattens but a linear relationship is retained. The slopes beyond 1.2 ps show a weak dependence on pump fluence (Figure 4b), suggesting that annihilation still enhances e^--h^+ recombination beyond the first ps but is not the dominant process anymore.
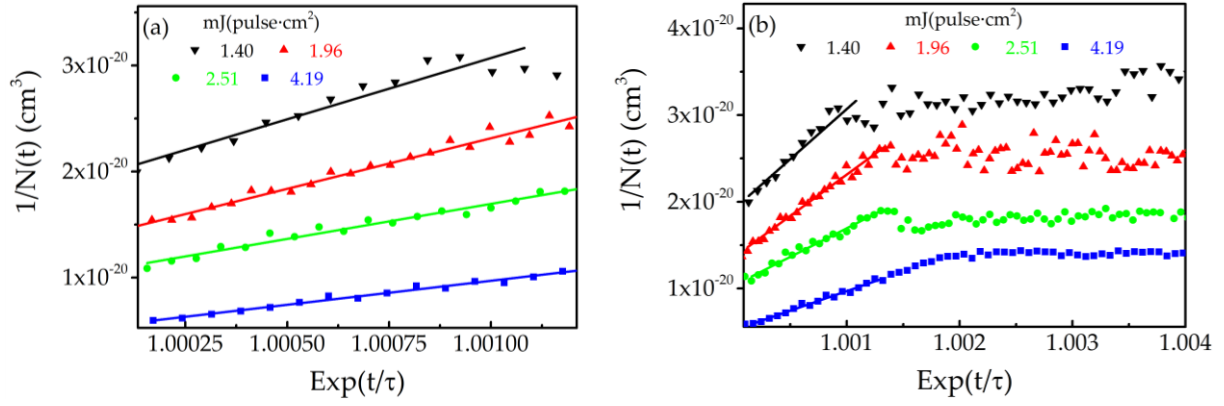
Figure 4. Annihilation graphs derived from the 570 nm spectra, showing the (a) first 1.2 ps, and (b) an extended delay time, indicating that annihilation is only dominant in the first ~1.2 ps. Symbols represent experimental data while solid straight lines are linear fits of data corresponding to delay times up to 1.2 ps. A weighted average value of 1.5 ns was used for τ.

The data in Figure 4a was fitted using Equation (2), giving for all fluence values an annihilation rate constant, γ_{eea}, of $(7.60 \pm 0.02) \times 10^{-9}$ cm^{3}s^{-1}. The dominance of EEA being limited mainly to the first ps can be explained by the high density of traps in hematite that depletes the exciton population within a few ps. Additionally, the small annihilation constant is indicative of a small exciton diffusion coefficient, D. For a diffusion-limited three-dimensional (3D) system, D and γ_{eea} relate through $\gamma_{eea} = 4\pi R_a D$, where R_a is the annihilation radius, representing the average separation at which two excitons may undergo annihilation[46]. The exciton diffusion length, L_D, given as $L_D = \sqrt{(D\tau)}$, implies a large exciton density would have to be created for diffusion-limited EEA to be observed. From the relations of γ_{eea} and L_D, we can express the EEA radius as $R_a = \gamma_{eea}\tau/4\pi L_D^2$. The exciton diffusion length can be approximated with the hole diffusion length since the diffusion of an exciton can be taken to consist of electron diffusion and hole diffusion, separately. Due to the wide range of reported hole diffusion lengths, we decided to calculate a range of possible annihilation radii, first considering L_D to be 2 nm[14] and lastly taking L_D to be 20 nm[15]. However, using 2 nm for the value of L_D yielded unrealistically large values of R_a whereas

using 20 nm for L_D, we obtained the annihilation radius as 2.3 nm. We also calculated the average distance between excitations to increase from 1.7 nm for a pump fluence of 4.19 mJ/(pulse·cm^2) to 2.5 nm for 1.40 mJ/(pulse·cm^2), estimating the gaps between neighbouring particles to occupy ~10% of the space. The annihilation radius is, therefore, greater than or approximately equal to the average distances between excitations for the fluences we considered. This explains the rapid $e^- $-$h^+$ recombination immediately after photoexcitation since adjacent excitons are formed, on average, within the annihilation radius of each other. It follows from these calculations that using 2 nm for the value of L_D would be an underestimation for our samples. We also note that in most articles where the value of 2-4 nm is reported as the hole diffusion length, the lifetimes reported are also much shorter (up to 2 orders of magnitude) than the values we obtained in this work.

From previous studies, it has been observed that EEA in a variety of materials takes place on fs–ps timescales[35, 47-50]. EEA has been shown to take place in other semiconductors of various dimensions, inorganic semiconductors, and in non-semiconductor materials such as conjugated polymers[51] and photosynthetic light-harvesting complexes[52-53]. The EEA rate constants of other 3D materials are comparable (within one order of magnitude) with that of hematite in the present study, for example, MEH-PPV (~10^{-8} cm^{3}s^{-1})[51], oligoaniline films (~10^{-10} cm^{3}s^{-1})[54], and the organic semiconductor PTCDA (~10^{-10} cm^{3}s^{-1})[55-56]. Higher EEA rates are common in materials with reduced dimensionality, where the probability of many-body interactions is high, such as bilayered tungsten disulfide (10^{-3} cm^2 s^{-1}) and monolayered materials like molybdenum diselenide (10^{-2} cm^2 s^{-1})[57].

4.2   Recombination pathways

We have previously carried out target analysis to demonstrate the various recombination channels in hematite following a pump pulse centred at 3.2 eV[20]. We extend the model here

to include an additional channel of EEA. A six-compartment target model, shown in Figure 5, was applied to the datasets to test the envisaged electron-hole recombination model. The pump pulse excites electrons to states within the conduction band (CB_m), i.e. above the conduction band minimum (CB_{min}). From CB_m, excited state electrons can relax to CB_{min} or be transferred to the FTO while holes also diffuse to the valence band maximum, both processes occurring at similar timescales for each fluence and under 500 fs across the four pump fluences. We also take into account that since the FTO valence band (FTO_{VB}) is more positive than that of Fe_2O_3, there is no hole diffusion into the FTO from hematite. However, electron flow into the FTO is allowed even though FTO_{CB} is more negative than the Fe_2O_3 conduction band minimum. This can be explained by electron excitation to 1.1 eV above CB_{min}, whereas the separation between the conduction bands of FTO and Fe_2O_3 is only ~0.5 eV. From CB_{min}, there are three possibilities. First, there is exciton formation and, subsequently, EEA in the first ps. As annihilation occurs, one exciton transfers its energy to the next exciton, which is then excited to a higher excited state, labeled CB_n, while the donor exciton relaxes to the ground state. The exciton promoted to CB_n is highly unstable and immediately relaxes to the ground state. These processes occur at an ultrafast timescale, which explains why EEA-assisted e^--h^+ recombination is a very fast process. In our target analysis, we constrained the EEA process (process (ii)) to 1 ps, as motivated by the annihilation graphs (Figure 6). Constraining already known rate constants helps in simplifying the model and ultimately yields more accurate values for the transitions whose rate constants are not predetermined. A competing process occurring nearly as fast is electron trapping by midgap states (process (iii)), and the trapped electrons either undergo ESA back to the conduction band (process (iv)) or recombine with the valence band holes (process (v)). It is, however, important to note that the trapping process is more dominant after the first ps, hence a reduced exciton concentration leading to negligible EEA. Lastly, the excited state

21

electrons initially transferred to the FTO can also be transferred back to the hematite conduction band and eventually recombine with the valence band holes (processes (vi)). These processes occur at much longer timescales – in the order of ns. Inverses of the rate constants obtained from target analysis are summarised in Table 2. These inversed rate constants present the characteristic times of electron and/or hole relaxation or e^{-}-h^{+} recombination between the respective compartments.
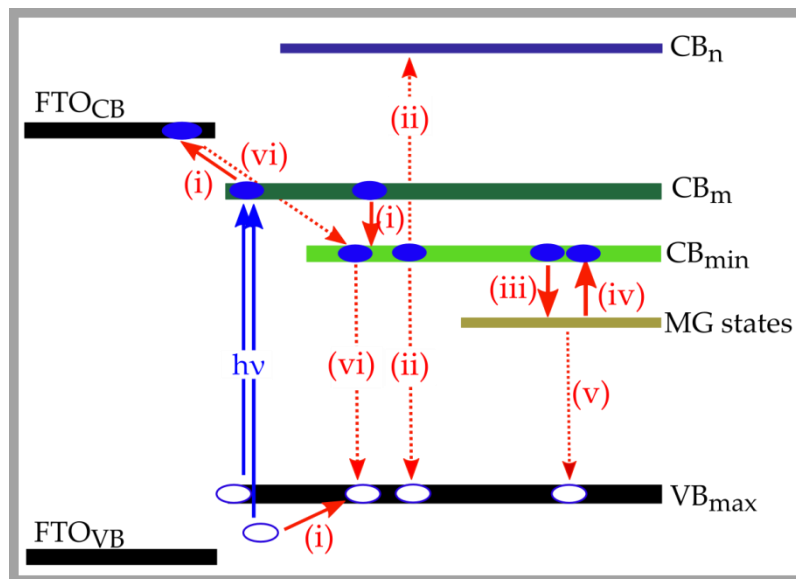
Figure 5. Recombination model following pump excitation of 3.2 eV (solid blue arrows marked hν) in a hematite sample deposited on FTO. Filled ellipses represent electrons while empty ellipses represent holes. Recombinations of e^{-}-h^{+} pairs involving valence band holes are represented by red dashed arrows (processes (ii), (iv) and (v)) while the other possible electron and hole dynamics are represented by red solid arrows (processes (i), (iii) and (v)). The model is not drawn to scale.

Table 2. Lifetimes of the different processes following target analysis applied to the kinetic model shown in Figure 5.

	1.40 mJ/(pulse·cm^2)	1.96 mJ/(pulse·cm^2)	2.51 mJ/(pulse·cm^2)	4.19 mJ/(pulse·cm^2)
$\tau_{(i)}$	470 fs	389 fs	322 fs	259 fs
$\tau_{(ii)}$	1.0 ps	1.0 ps	1.0 ps	1.0 ps
$\tau_{(iii)}$	2.6 ps	2.2 ps	2.7 ps	2.1 ps
$\tau_{(iv)}$	12.5 ps	10.9 ps	11.2 ps	9.3 ps
$\tau_{(v)}$	90.2 ps	87.6 ps	78.8 ps	80.1 ps
$\tau_{(vi)}$	5.5 ns	4.7 ns	4.7 ns	3.2 ns

5 Conclusions

Fluence-dependent transient-absorption measurements were carried out on nanostructured hematite thin films. The data displayed similar spectral features across the excitation fluences. An inverse relationship between pump excitation fluence and decay lifetime on fs-ns timescales was observed. Higher excitation fluences caused faster decay rates, attributed to exciton-exciton annihilation. Annihilation calculations confirmed that exciton-exciton annihilation is dominant at initial timescales, particularly during the first picosecond after photo-excitation. Probe wavelength dependent decay rates indicate that trap-assisted recombination of photo-created electrons and holes occurs. We have presented a kinetic model for e^--h^+ recombination in the presence of EEA and a high density of states. Since EEA contributes to e^--h^+ recombination, the recombination can be slowed down in a material by limiting EEA, for example by incorporating a high density of traps that can deplete the exciton concentration. Care should be taken to create a balance between slowing down EEA without significantly facilitating trap-assisted recombination. Additionally, our study

indicates the importance of taking nonlinear processes such as bimolecular Auger recombination into account when investigating hematite and other semiconductors under high fluences.

Acknowledgments

Supporting information

Four Supporting Figures: 3D spectra for all four fluences; EADS for all four fluences; graphs used to check for the presence of Auger recombination; and illustration of wavelength-dependent decay for the four fluences.

References

1. Fujishima, A.; Honda, K., Electrochemical Photolysis of Water at a Semiconductor Electrode. *Nature* **1972**, *238*, 37-38.

2. Augustyński, J.; Alexander, B.; Solarska, R., Metal Oxide Photoanodes for Water Splitting. *Photocatalysis* **2011**, 1-38.

3. Alexander, B. D.; Kulesza, P. J.; Rutkowska, I.; Solarska, R.; Augustynski, J., Metal Oxide Photoanodes for Solar Hydrogen Production. *J. Matter. Chem.* **2008**, *18*, 2298-2303.

4.   Asahi, R.; Morikawa, T.; Ohwaki, T.; Aoki, K.; Taga, Y., Visible-Light Photocatalysis in Nitrogen-Doped Titanium Oxides. *Science* **2001**, *293*, 269-271.

5.   Ravensbergen, J.; Abdi, F. F.; van Santen, J. H.; Frese, R. N.; Dam, B.; van de Krol, R.; Kennis, J. T. M., Unraveling the Carrier Dynamics of $BiVO_4$: A Femtosecond to Microsecond Transient Absorption Study. *J. Phys. Chem. C* **2014**, *118*, 27793-27800.

6.   Pesci, F. M.; Cowan, A. J.; Alexander, B. D.; Durrant, J. R.; Klug, D. R., Charge Carrier Dynamics on Mesoporous WO_3 during Water Splitting. *J. Phys. Chem. Lett.* **2011**, *2*, 1900-1903.

7.   Liu, M.; Nam, C.-Y.; Black, C. T.; Kamcev, J.; Zhang, L., Enhancing Water Splitting Activity and Chemical Stability of Zinc Oxide Nanowire Photoanodes with Ultrathin Titania Shells. *J. Phys. Chem. C* **2013**, *117*, 13396-13402.

8.   Kuciauskas, D.; Freund, M. S.; Gray, H. B.; Winkler, J. R.; Lewis, N. S., Electron Transfer Dynamics in Nanocrystalline Titanium Dioxide Solar Cells Sensitized with Ruthenium or Osmium Polypyridyl Complexes. *J. Phys. Chem. B* **2001**, *105*, 392-403.

9.   Walter, M. G.; Warren, E. L.; McKone, J. R.; Boettcher, S. W.; Mi, Q.; Santori, E. A.; Lewis, N. S., Solar Water Splitting Cells. *Chem. Rev.* **2010**, *110*, 6446-6473.

10.   Liu, C.; Yang, Y.; Li, J.; Chen, S.; Li, W.; Tang, X., An in Situ Transformation Approach for Fabrication of $BiVO_4$/WO_3 Heterojunction Photoanode with High Photoelectrochemical Activity. *Chem. Eng. J.* **2017**.

11.   Gilbert, B.; Frandsen, C.; Maxey, E. R.; Sherman, D. M., Band-Gap Measurements of Bulk and Nanoscale Hematite by Soft X-Ray Spectroscopy. *Phys. Rev. B* **2009**, *79*.

12.   Marusak, L. A.; Messier, R.; White, W. B., Optical Absorption Spectrum of Hematite, α-Fe_2O_3 near IR to UV. *J. Phys. Chem. Solids* **1980**, *41*, 981.

13.   Dare-Edwards, M. P.; Goodenough, J. B.; Hamnett, A.; Trevellick, P. R., Electrochemistry and Photoelectrochemistry of Iron(III) Oxide. *J. Chem. Soc. Faraday Trans.* **1983**, *79*, 2027-2041.

14.   Kennedy, J. H.; Frese, K. W., Photooxidation of Water at α-Fe_2O_3 Electrodes. *J. Electrochem. Soc.* **1978**, *125*, 709-714.

15.   Hamann, T. W., Splitting Water with Rust: Hematite Photoelectrochemistry. *Dalton Trans.* **2012**, *41*, 7830-7834.

16.   Sivula, K.; Le Formal, F.; Gratzel, M., Solar Water Splitting: Progress Using Hematite (α-Fe_2O_3) Photoelectrodes. *ChemSusChem* **2011**, *4*, 432-49.

17.   Cherepy, N. J.; Liston, D. B.; Lovejoy, J. A.; Deng, H.; Zhang, J. Z., Ultrafast Studies of Photoexcited Electron Dynamics in γ-and α-Fe_2O_3 Semiconductor Nanoparticles. *J. Phys. Chem. B* **1998**, *102*, 770-776.

18.   Franking, R.; Li, L.; Lukowski, M. A.; Meng, F.; Tan, Y.; Hamers, R. J.; Jin, S., Facile Post-Growth Doping of Nanostructured Hematite Photoanodes for Enhanced Photoelectrochemical Water Oxidation. *Energy Environ. Sci.* **2013**, *6*, 500-512.

19.   Anandan, S.; Ohashi, N.; Miyauchi, M., ZnO-Based Visible-Light Photocatalyst: Band-Gap Engineering and Multi-Electron Reduction by Co-Catalyst. *Appl. Catal. B: Environ.* **2010**, *100*, 502-509.

20.   Paradzah, A. T.; Diale, M.; Maabong, K.; Krüger, T. P., Use of Interfacial Layers to Prolong Hole Lifetimes in Hematite Probed by Ultrafast Transient Absorption Spectroscopy. *Physica B: Condens. Matter.* **2018**, *535*, 138--142.

21.   Le Formal, F.; Pendlebury, S. R.; Cornuz, M.; Tilley, S. D.; Grätzel, M.; Durrant, J. R., Back Electron–Hole Recombination in Hematite Photoanodes for Water Splitting. *J. Am. Chem. Soc.* **2014**, *136*, 2564-2574.

22.   Huang, Z., et al., In Situ Probe of Photocarrier Dynamics in Water-Splitting Hematite (α-Fe$_2$O$_3$) Electrodes. *Energy Environ. Sci.* **2012**, *5*, 8923.

23.   Shen, S.; Kronawitter, C. X.; Wheeler, D. A.; Guo, P.; Lindley, S. A.; Jiang, J.; Zhang, J. Z.; Guo, L.; Mao, S. S., Physical and Photoelectrochemical Characterization of Ti-Doped Hematite Photoanodes Prepared by Solution Growth. *J. Mater. Chem. A* **2013**, *1*, 14498-14506.

24.   Sorenson, S.; Driscoll, E.; Haghighat, S.; Dawlaty, J. M., Ultrafast Carrier Dynamics in Hematite Films: The Role of Photoexcited Electrons in the Transient Optical Response. *J. Phys. Chem. C* **2014**, *118*, 23621-23626.

25.   Wheeler, D. A.; Wang, G.; Ling, Y.; Li, Y.; Zhang, J. Z., Nanostructured Hematite: Synthesis, Characterization, Charge Carrier Dynamics, and Photoelectrochemical Properties. *Energy Environ. Sci.* **2012**, *5*, 6682.

26.   Ling, Y.; Wang, G.; Wheeler, D. A.; Zhang, J. Z.; Li, Y., Sn-Doped Hematite Nanostructures for Photoelectrochemical Water Splitting. *Nano Lett.* **2011**, *11*, 2119-2125.

27.   Pendlebury, S. R.; Wang, X.; Le Formal, F.; Cornuz, M.; Kafizas, A.; Tilley, S. D.; Gratzel, M.; Durrant, J. R., Ultrafast Charge Carrier Recombination and Trapping in Hematite Photoanodes under Applied Bias. *J. Am. Chem. Soc.* **2014**, *136*, 9854-7.

28.   Snellenburg, J. J.; Laptenok, S. P.; Seger, R.; Mullen, K. M.; van Stokkum, I. H., Glotaran: A Java-Based Graphical User Interface for the R Package Timp. *J. Stat. Softw.* **2012**, *49*, 1--22.

29.   Becker, U.; Hochella, M. F.; Apra, E., The Electronic Structure of Hematite {001} Surfaces: Applications to the Interpretation of STM Images and Heterogeneous Surface Reactions. *American Mineralogist* **1996**, *81*, 1301-1314.

30.   Liao, P.; Carter, E. A., Optical Excitations in Hematite (α-Fe$_2$O$_3$) via Embedded Cluster Models: A CAPST2 Study. *J. Phys. Chem. C* **2011**, *115*, 20795-20805.

31.   Hayes, D.; Hadt, R. G.; Emery, J. D.; Cordones, A. A.; Martinson, A. B.; Shelby, M. L.; Fransted, K. A.; Dahlberg, P. D.; Hong, J.; Zhang, X., Electronic and Nuclear Contributions to Time-Resolved Optical and X-Ray Absorption Spectra of Hematite and Insights into Photoelectrochemical Performance. *Energy Environ. Sci.* **2016**, *9*, 3754-3769.

32.   Cheng, K.; He, Y.; Miao, Y.; Zou, B.; Wang, Y.; Wang, T.; Zhang, X.; Du, Z., Quantum Size Effect on Surface Photovoltage Spectra: α-Fe$_2$O$_3$ Nanocrystals on the Surface of Monodispersed Silica Microsphere. *J. Phys. Chem. B* **2006**, *110*, 7259-7264.

33.   He, Y.; Miao, Y.; Li, C.; Wang, S.; Cao, L.; Xie, S.; Yang, G.; Zou, B.; Burda, C., Size and Structure Effect on Optical Transitions of Iron Oxide Nanocrystals. *Phys. Rev. B* **2005**, *71*, 125411.

34.   Barroso, M.; Mesa, C. A.; Pendlebury, S. R.; Cowan, A. J.; Hisatomi, T.; Sivula, K.; Grätzel, M.; Klug, D. R.; Durrant, J. R., Dynamics of Photogenerated Holes in Surface Modified α-Fe$_2$O$_3$ Photoanodes for Solar Water Splitting. *Proc. Natl. Acad. Sci.* **2012**, *109*, 15640-15645.

35.   Wheeler, D. A.; Huang, J.-A.; Newhouse, R. J.; Zhang, W.-F.; Lee, S.-T.; Zhang, J. Z., Ultrafast Exciton Dynamics in Silicon Nanowires. *J. Phys. Chem. Lett.* **2012**, *3*, 766-771.

36.   Joly, A. G.; Williams, J. R.; Chambers, S. A.; Xiong, G.; Hess, W. P.; Laman, D. M., Carrier Dynamics in α-Fe$_2$O$_3$ (0001) Thin Films and Single Crystals Probed by Femtosecond Transient Absorption and Reflectivity. *J. Appl. Phys.* **2006**, *99*, 053521.

37.   Dotan, H.; Sivula, K.; Grätzel, M.; Rothschild, A.; Warren, S. C., Probing the Photoelectrochemical Properties of Hematite (α-Fe$_2$O$_3$) Electrodes Using Hydrogen Peroxide as a Hole Scavenger. *Energy Environ. Sci.* **2011**, *4*, 958-964.

38.   Pendlebury, S. R.; Barroso, M.; Cowan, A. J.; Sivula, K.; Tang, J.; Gratzel, M.; Klug, D.; Durrant, J. R., Dynamics of Photogenerated Holes in Nanocrystalline α-Fe$_2$O$_3$ Electrodes

for Water Oxidation Probed by Transient Absorption Spectroscopy. *Chem. Commun. (Camb.)* **2011**, *47*, 716-8.

39.   Barroso, M.; Cowan, A. J.; Pendlebury, S. R.; Grätzel, M.; Klug, D. R.; Durrant, J. R., The Role of Cobalt Phosphate in Enhancing the Photocatalytic Activity of α-Fe_2O_3 toward Water Oxidation. *J. Am. Chem. Soc.* **2011**, *133*, 14868-14871.

40.   Sherman, D. M.; Waite, T. D., Electronic Spectra of Fe^{3+} Oxides and Oxide Hydroxides in the near IR to near UV. *Am. Mineral.* **1985**, *70*, 1262-1269.

41.   Yuan, L.; Huang, L., Exciton Dynamics and Annihilation in WS_2 2D Semiconductors. *Nanoscale* **2015**, *7*, 7402-7408.

42.   You, Y.; Zhang, X.-X.; Berkelbach, T. C.; Hybertsen, M. S.; Reichman, D. R.; Heinz, T. F., Observation of Biexcitons in Monolayer WSe_2. *Nat Phys* **2015**, *11*, 477-481.

43.   Ma, Y.-Z.; Valkunas‡, L.; Dexheimer §, S.; Fleming, G., Ultrafast Exciton Dynamics in Semiconducting Single-Walled Carbon Nanotubes. *Mol. Phys.* **2006**, *104*, 1179-1189.

44.   Mikhnenko, O. V.; Blom, P. W. M.; Nguyen, T.-Q., Exciton Diffusion in Organic Semiconductors. *Energy Environ. Sci.* **2015**, *8*, 1867-1888.

45.   Yu, Y.; Yu, Y.; Xu, C.; Barrette, A.; Gundogdu, K.; Cao, L., Fundamental Limits of Exciton-Exciton Annihilation for Light Emission in Transition Metal Dichalcogenide Monolayers. *Phys. Rev. B* **2016**, *93*, 201111.

46.   Hedley, G. J.; Ruseckas, A.; Samuel, I. D., Light Harvesting for Organic Photovoltaics. *Chem. Rev.* **2016**, *117*, 796-837.

47.   Jundt, C.; Klein, G.; Sipp, B.; Le Moigne, J.; Joucla, M.; Villaeys, A., Exciton Dynamics in Pentacene Thin Films Studied by Pump-Probe Spectroscopy. *Chem. Phys. Lett.* **1995**, *241*, 84-88.

48.	Sun, D.; Rao, Y.; Reider, G. A.; Chen, G.; You, Y.; Brézin, L.; Harutyunyan, A. R.; Heinz, T. F., Observation of Rapid Exciton–Exciton Annihilation in Monolayer Molybdenum Disulfide. *Nano Lett.* **2014**, *14*, 5625-5629.

49.	Wang, S.; Khafizov, M.; Tu, X.; Zheng, M.; Krauss, T. D., Multiple Exciton Generation in Single-Walled Carbon Nanotubes. *Nano Lett.* **2010**, *10*, 2381-2386.

50.	Gulbinas, V.; Valkunas, L.; Kuciauskas, D.; Katilius, E.; Liuolia, V.; Zhou, W.; Blankenship, R. E., Singlet-Singlet Annihilation and Local Heating in FMO Complexes. *J. Phys. Chem.* **1996**, *100*, 17950-17956.

51.	Lewis, A. J.; Ruseckas, A.; Gaudin, O. P. M.; Webster, G. R.; Burn, P. L.; Samuel, I. D. W., Singlet Exciton Diffusion in MEH-PPV Films Studied by Exciton–Exciton Annihilation. *Org. Electron.* **2006**, *7*, 452-456.

52.	Elnour, H. M.; Dietzel, L.; Ramanan, C.; Büchel, C.; Van Grondelle, R.; Krüger, T. P., Energy Dissipation Mechanisms in the FCPb Light-Harvesting Complex of the Diatom Cyclotella Meneghiniana. *Biochim. Biophys. Acta* **2018**, *1859*, 1151-1160.

53.	Gruber, J. M.; Chmeliov, J.; Krüger, T. P.; Valkunas, L.; Van Grondelle, R., Singlet–Triplet Annihilation in Single LHCII Complexes. *PCCP* **2015**, *17*, 19844-19853.

54.	Faulques, E.; Ivanov, V.; Jonusauskas, G.; Athalin, H.; Pyshkin, O.; Wéry, J.; Massuyeau, F.; Lefrant, S., Ultrafast Photoluminescence Spectroscopy of Exciton-Exciton Annihilation in Oligoaniline Films with Nanoscale Ordering. *Phys. Rev. B* **2006**, *74*, 075202.

55.	Mikhnenko, O. V.; Blom, P. W.; Nguyen, T.-Q., Exciton Diffusion in Organic Semiconductors. *Energy Environ. Sci.* **2015**, *8*, 1867-1888.

56.	Engel, E.; Leo, K.; Hoffmann, M., Ultrafast Relaxation and Exciton–Exciton Annihilation in PTCDA Thin Films at High Excitation Densities. *Chem. Phys.* **2006**, *325*, 170-177.

57.	Kumar, N.; Cui, Q.; Ceballos, F.; He, D.; Wang, Y.; Zhao, H., Exciton-Exciton Annihilation in MoSe$_2$ Monolayers. *Phys. Rev. B* **2014**, *89*, 125427.

TOC GRAPHICS